ORIGINAL ARTICLE

Experimental study of long wave dynamics in the presence of two offshore islands

Adam S. Keen[1] [ID] **· Patrick J. Lynett[1]**

Abstract
Following the 2010 Mentawai tsunami, observations in Sumatra by Hill et al. (J Geophys Res Solid Earth, 2012. https://doi.org/10.1029/2012jb009159) noted enhanced tsunami runup in coastal areas behind island chains. Many local communities in the region, however, falsely believed that islands provide shelter against tsunami waves. The present study aims to capture when and how island chains are amplifiers of wave energy in the coastal areas they shadow, which is often where coastal communities thrive. Physical modeling was carried out in the Directional Wave Basin at the Oregon State University O.H. Hinsdale Wave Research Laboratory. The experiment included four island configurations and three different waveforms a: solitary wave, error function wave and a leading depression N-wave. Results suggest that island chains can act as wave amplifiers, indicating potential amplification in both shoreline runup and current velocity. The amplification is, however, not consistent with every waveform. Also, in some cases, the impact of the offshore islands led to a reduction in coastal impacts. This result suggests that the offshore waveform plays an important role in the wave dynamics between the islands and on the wave uprush directly behind the islands.

Keywords Tsunamis · Long wave dynamics · Sumatra islands · Long wave runup · Physical modeling

List of symbols
d Water depth (m)
H Wave height (m)
H_1 Wave height estimated at resistance WG 01 (m)
R_x Wave runup maximum magnitude (where X references Configuration A–E) (m)
r_x Wave runup distance (where X references Configuration A–E) (m)
T Wave time scale (s)

✉ Adam S. Keen
   adamkeen@usc.edu

   Patrick J. Lynett
   plynett@usc.edu

[1]   Sonny Astani Department of Civil and Environmental Engineering, University of Southern California, Los Angeles, USA

U_x	Current velocity maximum magnitude (where X references Configuration A–E) (m/s)
u_x	Current velocity time series (where X references Configuration A–E) (m/s)
X	Cross-shore distance in direction wave basin coordinates (m)
x	Cross-shore location in direction wave basin coordinates (m)
Y	Alongshore distance in direction wave basin coordinates (m)
y	Alongshore location in direction wave basin coordinates (m)
Z	Vertical elevation in direction wave basin coordinates (m)
z	Vertical location in direction wave basin coordinates (m)
η	Surface elevation (m)
η_{max}	Maximum surface elevation (m)

1 Introduction

The 2004 Indonesian tsunami in Banda Aceh greatly increased the public's understanding of tsunamis through video and photographic documentation of the destruction [2, 3]. Since the 2004 Indonesian tsunami, significant advances have been made in the operational response to tsunamis [4–8]. For example, the National Ocean and Atmospheric Administration (NOAA) expanded their original six Deep-ocean Assessment and Reporting of Tsunami (DART) stations to a full network of 39 stations in 2008. NOAA's intent was to expand the global early warning and real-time reporting capabilities of tsunamis in the open ocean [9]. Stefanakis et al. [10] suggests early warning along with preparedness remains the only effective countermeasure to save lives during a tsunami event.

To supplement these types of warning products, and to understand site-specific tsunami hazard with greater precision, the effects of local bathymetry and topographic features must be captured. In some cases, communities may have an under-developed understanding of tsunami flow phenomena that are counterintuitive, potentially leading at-risk residences to a false sense of safety. During the 1992 Flores tsunami, residences of Babi Island believed that locating their villages on the backside of the island would protect them from incoming tsunami waves [11, 12]. Yet, the 1992 tsunami destroyed both villages. Lab experiments conducted by Briggs et al., as well as numerical computations by Liu et al., showed that long waves can amplify runup on the lee side of an island [13, 14].

Following the 2010 Mentawai tsunami, observations by Hill et al. [1] have shown enhanced tsunami runup in coastal areas in the Mentawai Island Chains off Sumatra. In fact, Satake et al. [15] recorded one of the highest flow depths in their survey, immediately behind the island of Pulau Sibigau. Researchers have a poor understanding of why this amplification occurs behind the island. Limited experimental data exists to better understand the tsunami flow phenomena in the presence of island chains.

The present study aims to capture when and how island chains are amplifiers of wave energy in the coastal areas they shadow, which is often where coastal communities thrive. This paper is organized into four main sections. Section 2 will summarize the experimental setup of physical modeling carried out in the Directional Wave Basin (DWB) at the Oregon State University (OSU) O.H. Hinsdale Wave Research Laboratory. Section 3 discusses the data collection, post-processing and results of runup measurements taken directly on the conical islands during the experiment. Runup on the planar beach shoreward of the islands is analyzed in Sect. 4. Section 5 will discuss flow velocity data taken just shoreward of the islands. Conclusions are presented in Sect. 6.

2 Experimental setup

2.1 General arrangement and bathymetry

Physical modeling was carried out in the DWB at the OSU O.H. Hinsdale Wave Research Laboratory. The basin dimensions are 48.8 m by 26.5 m. At the far end of the basin is a snake-type wavemaker made of 29 boards, each capable of producing a 2.1 m long stroke. A planar beach was installed at the far end of the basin. The beach starts at approximately x = 22.9 m and extends upward at a slope of 1:10 to the end of the tank. A conceptual layout of the experimental setup is provided in Fig. 1.

Four different conical features were used to model conical islands in the wave basin: two full cones and two truncated cones. The islands were fabricated out of a steel frame and covered in sheet metal panels welded together. While all four cones had side slopes of 27°, base dimensions and truncation heights varied. Base diameters of the two full cones were 3.2 m and 4.0 m, respectively. The height of the 3.2 m truncated cone was 0.30 m while the height of the 4.0 m cone was 0.5 m.

A total of five cone configurations (Configuration A–E) were modeled within the basin. The layouts are shown in Fig. 1 and summarized in Table 1. Configuration A and B are idealized cross-shore oriented configurations of islands located off the western coast of Pulau Pagai-selatan in the Mentawai Islands. Hill et al. and Stefanakis et al. noted particularly high runup amplification behind these islands [1, 10].

The Mentawai Islands for Configuration A and B were modeled with the 3.2 and 4.0 diameter full cones. To locate the cones within the tank for Configuration A, a benchmark was surveyed at (x = 21.6 m, y = 0.0 m) along the toe of the beach. The 4.0 m cone was placed first by aligning the shoreward limit of the cone base tangentially with the benchmark at x = 21.6 m. The island was then centered along y = 0 m before being bolted to the basin floor. Next, the 3.2 m cone was centered along y = 0.0 m offshore of the 4.0 m cone and placed so that the two cones met tangentially at approximately
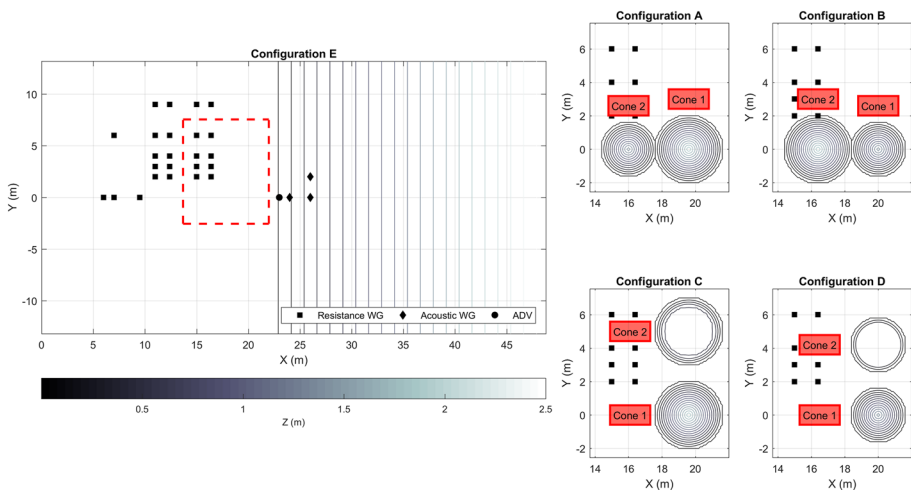

Fig. 1 Experimental setup of conical islands in directional wave basin

Table 1 Orientation and cone dimensions for Configuration A–E

Configuration	Orientation	Cone 1		Cone 2		Cone 1/2
		Base diameter (m)	Truncation height (m)	Base diameter (m)	Truncation height (m)	Base separation (m)
A	Cross-shore	4.0	–	3.2	–	0.0
B	Cross-shore	3.2	–	4.0	–	0.0
C	Alongshore	4.0	–	4.0	0.50	1.0
D	Alongshore	3.2	–	3.2	0.30	1.0
E	–	–	–	–	–	–

x = 17.6 m. Cones for Configuration B were placed in the same manner as Configuration A except that the 3.2 m cone was placed on the benchmark, followed by the 4.0 m cone.

Configuration C and D were also idealized configurations of long-shore oriented islands located off the western coast of Pulau Pagai-selatan. However, unlike Configuration A and B which idealized the Mentawai Islands in a cross-shore configuration with two full island, Configuration C and D modeled one full island and one truncated island oriented in an alongshore orientation. The truncation allowed the authors to model the complex wave interaction between the full cone (located along x = 0 m), wave overtopping and submerged features.

The cones for Configuration C were largely placed in the tank in the same manner as Configuration A. The 4.0 m cone was placed first by aligning the shoreward limit of the cone base tangentially with the benchmark at x = 21.6 m. The island was then centered along y = 0 m before being bolted to the floor. A second benchmark was then surveyed at (x = 21.6 m, y = 5.0 m). The 4.0 m truncated was aligned with the benchmark at x = 21.6 m and centered along y = 5.0 m before being bolted to the floor. Configuration D differs from Configuration C in that it uses the smaller 3.2 m full and truncated cone. The second benchmark for this configuration is also located at (x = 21.6 m, y = 4.2 m).

A no-island-scenario was modeled for comparison between Configuration A–D. This scenario is included in Fig. 1 and Table 1 as Configuration E. This Configuration E acts as a control, or a baseline, scenario.

2.2 Instrumentation

A suite of instruments was installed in the basin prior to filling the tank with water. The locations of the in situ instruments are shown in Fig. 1 and summarized in Table 2. Four self-calibrating resistance type wave gauges were installed close to the wavemaker to measure the free-surface elevation produced by the wavemaker paddle. Resistance Wave Gauge (WG) 01, 02 and 04 were installed approximately along the centerline of the tank locations of (x = 5.84 m, y = −0.02 m), (x = 7.05 m, y = −0.04 m) and (x = 9.48 m, y = −0.03 m), respectively. Resistance WG 03 was located at (x = 7.05 m, y = 5.97 m), shore parallel to Resistance WG 02.

To measure the complex wave patterns around the island, two sets of five resistance wave gauges were mounted to the base of the instrumentation carriage. After each wave and water level condition was run twice, the bridge was moved to collect a second set of free-surface elevation measurements. In Fig. 1, these wave gauges can be

Table 2 Location of in situ instruments in directional wave basin (DWB)	Instrument ID	X (m)	Y (m)	Z (m)
	Resistance wave gauge 01	5.84	− 0.02	–
	Resistance wave gauge 02	7.05	− 0.04	–
	Resistance wave gauge 03	7.05	5.97	–
	Resistance wave gauge 04	9.48	− 0.03	–
	Resistance wave gauge 05	11.00	1.97	–
	Resistance wave gauge 06	10.99	2.98	–
	Resistance wave gauge 07	10.98	4.11	–
	Resistance wave gauge 08	10.99	5.97	–
	Resistance wave gauge 09	10.98	9.03	–
	Resistance wave gauge 10	12.42	2.00	–
	Resistance wave gauge 11	12.43	2.99	–
	Resistance wave gauge 12	12.44	4.03	–
	Resistance wave gauge 13	12.41	6.03	–
	Resistance wave gauge 14	12.39	8.99	–
	Resistance wave gauge 15	15.00	1.97	–
	Resistance wave gauge 16	14.99	2.98	–
	Resistance wave gauge 17	14.98	4.11	–
	Resistance wave gauge 18	14.99	5.97	–
	Resistance wave gauge 19	14.98	9.03	–
	Resistance wave gauge 20	16.42	2.00	–
	Resistance wave gauge 21	16.43	2.99	–
	Resistance wave gauge 22	16.44	4.03	–
	Resistance wave gauge 23	16.41	6.03	–
	Resistance wave gauge 24	16.39	8.99	–
	Acoustic doppler velocimeter	23.08	0.00	0.18
	Ultra-sonic wave gauge 01	24.06	− 0.02	1.19
	Ultra-sonic wave gauge 02	26.07	− 0.03	1.20
	Ultra-sonic wave gauge 03	26.05	1.98	1.23

identified as four sets of five wave gauges at mean cross-shore locations of x ~ 10.99 m, x ~ 12.42 m, x ~ 14.99 m and x ~ 16.42 m, respectively. The exact location of each wave gauge is summarized in Table 2. In the table, Resistance WG 05–14 are representative of the first bridge location and Resistance WG 15–24 are representative of the second bridge location.

A triangular metal frame was installed on the planar beach to measure the wave runup pattern shoreward of the island. Attached to the metal frame was an acoustic doppler velocimeter (ADV) and three ultra-sonic wave gauges. The ultra-sonic wave gauges measured the runup flow thickness while the ADV measured fluid velocities. The ADV and Ultra-Sonic WG 01 and 02 were installed approximately along the cen-terline of the tank locations of (x = 23.00 m, y = 0.00 m, z = 0.18 m), (x = 24.06 m, y = − 0.02 m, z = 1.19 m) and (x = 26.07 m, y = − 0.03 m, z = 1.20 m), respectively. Ultra-Sonic WG 03 was located at (x = 26.05 m, y = 1.98 m, z = 1.23 m), shore parallel with Ultra-Sonic WG 02.

2.3 Wave and water level conditions

Five different wave boundary conditions were modeled in the DWB. These included a solitary wave with three different wave heights (H = 0.06 m, 0.10 m, 0.14 m), an error function wave and a leading depression N-wave, which is termed the "n_{max}" wave. Scaled wave conditions are shown in Fig. 2. Target and estimated solitary heights for each water level are shown in Table 3. Note that there is a slight difference between target and estimated wave heights. Briggs et al. [13] attribute the losses in the mechanical generation of the wave to gaps between the floor and the wavemaker that dissipate some of the wave energy.

Experimental researchers often model runup of tsunamis onto a sloping beach by imposing a solitary wave boundary condition. A solitary wave is advantageous due to its permanent and stable waveform. Many researches including Yeh et al. [12] point to the leading wave tsunami often emerging as solitons given sufficient propagation distance as validation for the use of the waveform. However, the solitary wave theory only applies to far field tsunamis since some time and/or propagation distance is required for the leading waves to emerge as solitons.

For near-field tsunamis (such as the one which occurred in the Mentawai Islands in 2010), however, a solitary wave may not be an appropriate approximation. For example, Madsen et al. [16] discusses eye witness reports of tsunamis breaking just before they reach the shoreline, providing photographic evidence within the paper. The authors point to instability of the wave front as the wave shoals and becomes nonlinear. Typically, the authors suggest, this happens close to the shore in very shallow water. In this region the wave does not have sufficient time or travel distance to develop leading solitons and instead develops into a breaking wave front.

For the reasoning provided by Madsen et al. [16], an error function wave was also modeled to include the breaking wave front in the tsunami dynamics around the conical islands. This wave is produced by the wavemaker as a single forward stroke lasting ~ 5 s, with the paddle time history described with an error function. The wave that was produced had a steep front and, in all cases modeled, breaks offshore of the islands in the constant water depth region. Unlike the solitary wave with a height dictated by wavemaker input, one unique feature of the error function wave is the wave height is dictated by the water depth. Steepness induced breaking controls the wave height development as the wave propagates away from the wavemaker. Error function wave heights for each water level are shown in Table 3. In Table 3 the error function wave height is measured from the zero-to-crest level.

In addition to the development of an undular breaking wave front developing in the nearshore for near-field tsunamis, some eyewitnesses and researchers have noted occurrences of an initial drawdown followed by a positive pulse of water as the tsunami arrives ashore. Tadepalli and Synolakis [17] attribute this feature to the generated long wave not having sufficient propagation distance to evolve. Tadepalli and Synolakis [17, 18] showed that the coastal manifestation of a tsunami is "N-wave like" and proved that the runup of leading depression N-waves is higher than the runup of leading elevation N-waves.

The "n_{max} wave" modeled in the DWB is intended to resemble the N-wave discussed by Tadepalli and Synolakis [17, 18]. The wave is produced by the wavemaker as a backward stoke lasting ~ 10 s and a forward stoke lasting ~ 6 s, where again, each of these paddle motions are prescribed with an error function. Like the error function wave, one
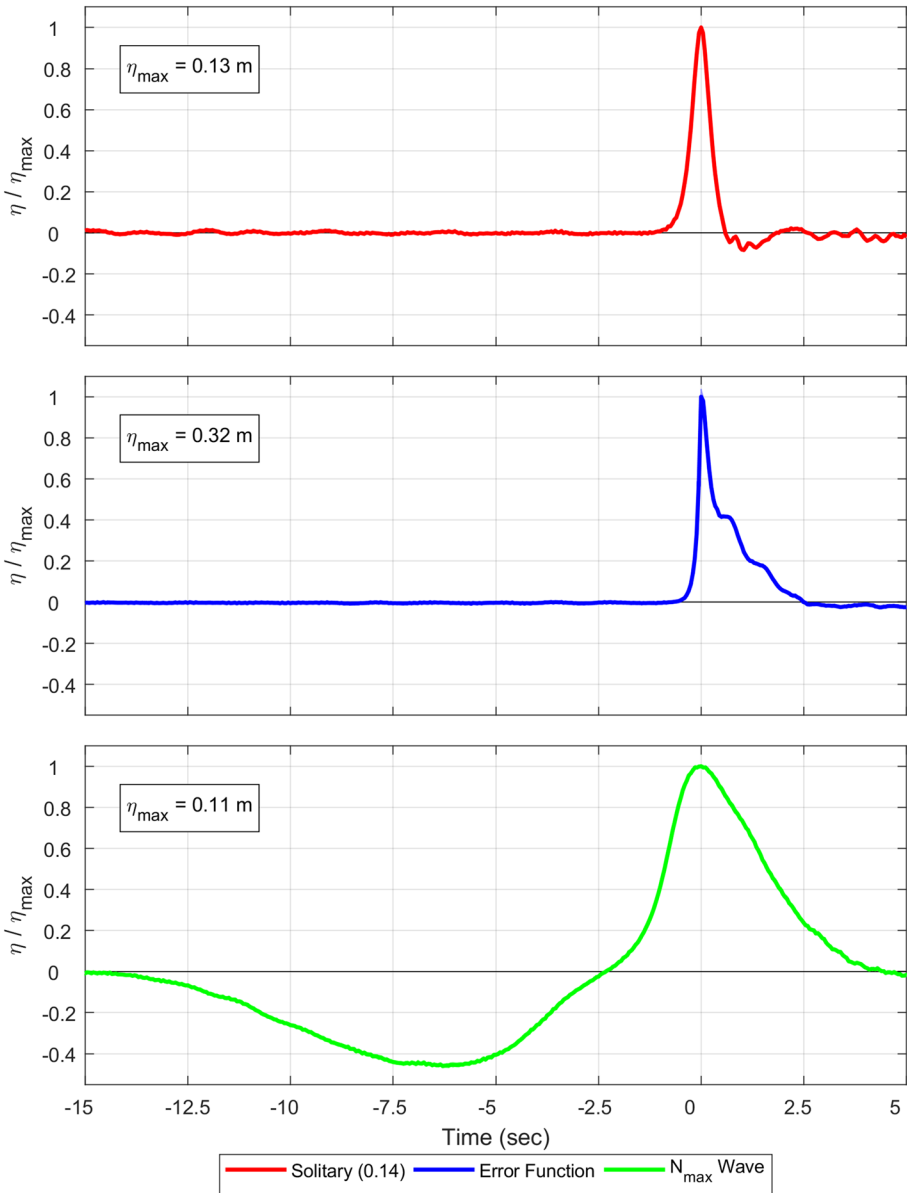
Fig. 2 Scaled boundary conditions used for the physical modeling: (top) solitary wave (H = 0.13 m), (middle) error function wave and (bottom) n_{max} wave. Surface elevation estimated at Resistance WG 01 for the 0.30 m water level

feature of the n_{max} wave is the wave height is dictated by the water depth. n_{max} wave heights for each water level are shown in Table 3 where the wave height is measured from the crest-to-trough. (Unlike the solitary and error function waves which are measured from the zero-to-crest level.)

Table 3 Summary of boundary conditions modeled in directional wave basin (DWB)

Waveform	d (m)	H (m)	H_1 (m)	H_1/d (−)	T (s)	r_E (m SWL)	U_E (m/s)
Solitary wave	0.23	0.06	0.05	0.22	1.9	1.4	0.37
Solitary wave	0.23	0.10	0.09	0.39	1.4	2.1	0.58
Solitary wave	0.23	0.14	0.13	0.57	1.1	2.7	0.74
Error function wave	0.23	–	0.21	0.91	5.0	3.1	0.77
N_{max} wave	0.23	–	0.13	0.57	16.0	2.9	1.00
Solitary wave	0.30	0.06	0.06	0.20	2.6	1.7	0.31
Solitary wave	0.30	0.10	0.09	0.30	1.9	2.5	0.49
Solitary wave	0.30	0.14	0.13	0.43	1.5	3.1	0.65
Error function wave	0.30	–	0.34	1.13	5.0	4.1	0.83
N_{max} wave	0.30	–	0.17	0.57	16.0	3.8	1.11
Solitary wave	0.50	0.06	0.06	0.12	4.5	2.0	0.23
Solitary wave	0.50	0.10	0.09	0.18	3.3	3.1	0.39
Solitary wave	0.50	0.14	0.13	0.26	2.7	3.9	0.52
Error function wave	0.50	–	0.34	0.68	5.0	6.9	0.91
N_{max} wave	0.50	–	0.20	0.40	16.0	5.7	1.03

The experiment also included three different water levels: 0.23 m, 0.30 m and 0.50 m. The lowest water level was dictated by the minimal amount of water required to cover the ADV. The 0.30 m and 0.50 m water levels were selected to cover a range of wave height to water depth ratios. The water depth (d), wave height (H), wave height estimated at Resistance WG 01 (H_1) and wave time scale (T) are summarized in Table 3. Time scales for the solitary wave are approximated using the approach presented by Synolakis [19]. When combined with the various wave conditions, a total of 15 wave and water level conditions were used for each island configuration. Each combination was repeated four times to allow for ensemble and band averaging during post-processing.

3 Conical island runup

3.1 Data collection

Conical island runup measurements were collected on Cone 1 (see Fig. 1) for Configurations A and Configuration B. To make this measurement, 24 vinyl measuring tapes were attached to the conical islands. Ten-degree spacing was used on the front and back ($330° \leq \theta \leq 30°$ and $150° \leq \theta \leq 210°$) while 20° spacing was used for the sides. The cones were orientated such that the 0° tape faced offshore while the 180° tape faced onshore. It is re-iterated that cone runup is only measured on the cone nearest to the shoreline; the runup on and wave evolution around the most-offshore cone should be similar to that investigated in Briggs et al. and we see no reason to repeat that effort [13]. Further information on the measurement procedure can be found in Appendix 1.

A total of four trials were completed for each wave type and water level configuration. Note that the cones were not perfectly symmetrical due to construction imperfections. To address this issue, the cone runup data was mirrored over the 0°–180° axis during post-processing. This resulted in a total of eight data points at each theta location from which

a mean, standard deviation and degrees of freedom were estimated. These three metrics were used to establish the 90% confidence bands which not only included variability in individual trials but also variability in cone shape because of the post-processing scheme.

To summarize the 30 combinations of cone configurations, waves, and water levels, a few representative runup points are used to characterize the cone runup. The schematic identifying the representative points is shown in Fig. 3. The three points used to describe the radial runup are: (R_1) $\theta = 0°$, (R_2) $\theta = 180°$ and (R_3) minimum runup elevation. These points were selected to best characterize unique features of the runup profile. Also note, radial runup shown in Fig. 3 is shown from 0° to 360°. However, results from 180° to 360° are the mirrored equivalent of results from 0° to 180° and are only included for visualization.

3.2 Results and discussion

When a tsunami approaches an island from deep water and propagates around a conical island, the wave undergoes a complex combination of processes including shoaling, refraction, diffraction, dissipation (e.g. wave breaking) and reflection. At each phase of wave propagation, segments of the wave experience a combination of processes because of local and antecedent differences in water depth. To help illustrate the processes, a conceptual description of the wave propagation from generation to final wave runup will be discussed below. A schematic summarizing the major phases of wave propagation is also shown in Fig. 4.
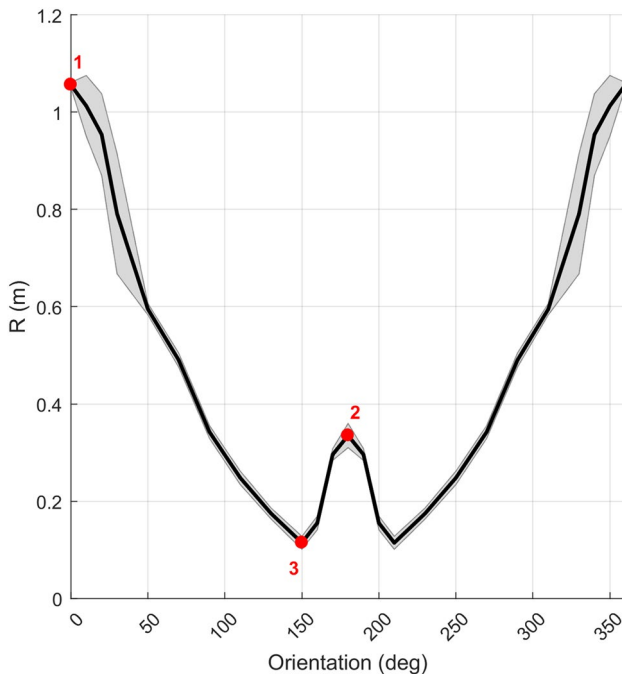
Fig. 3 Schematic shows the three repetitive points used to characterize the radial runup (R): (1) $\theta = 0°$, (2) $\theta = 180°$ and (3) minimum runup elevation. The shaded region shows representative 90% confidence bounds
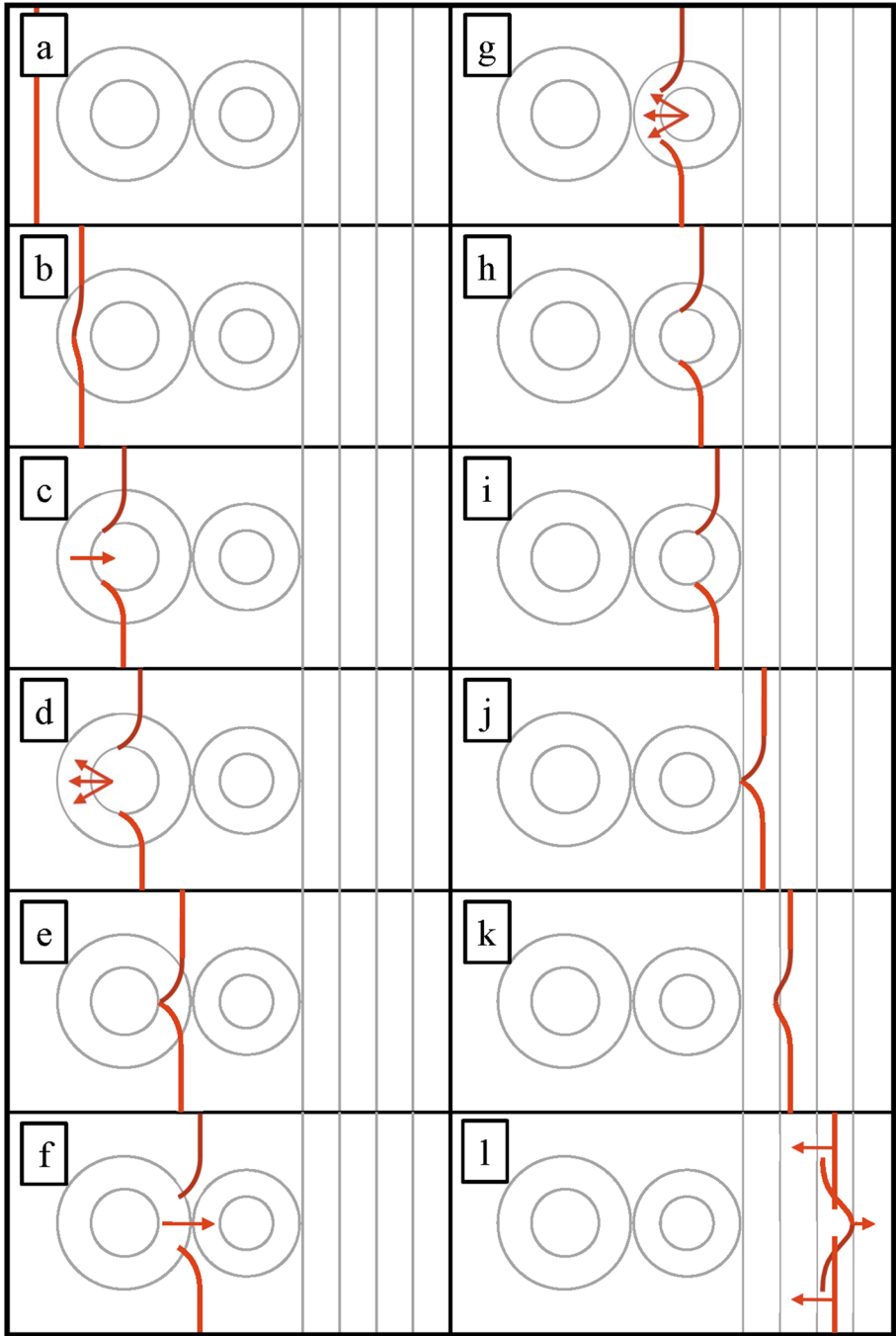
**Fig. 4** Schematic of wave runup for Configuration B

As the wavemaker generates a wave, (see panel a) the wave travels across the flat section of the DWB with a continuous uniform wave crest. Once the wave reaches the first offshore island (Fig. 4b), it will "feel" the bottom and sections of the wave in shallower water decrease in speed. The decrease in celerity will cause an increase in the wave amplitude (i.e. shoaling) as a decrease in celerity must be associated with an increase in energy density. Depth induced refraction will cause the wave crest to bend. Diffraction also transfers energy along the crest from areas of high wave energy density to low wave energy density.

As the wave continues forward, (Fig. 4c) a segment of the crest runs up the front side of the island while other segments bisect into two discontinuous crests that continue to propagate forward. Refraction, diffraction and shoaling continue to bend the wave crest and wrap the segments around the island as the wave runs down the front side of the island (see Fig. 4d). Once the two bisected segments meet on the back side of the island, (Fig. 4e) the two segments rejoin to produce the large back-of-the-island runup documented by Briggs et al. [13].

As the wave continues to propagate forward and the two fronts meet behind the offshore island, video of the wave field indicates that a stem starts to develop, produced by the two wave fronts rejoining. There is a complex interaction which occurs between the developing stem and propagating wave crests (see Fig. 4f). Wave dissipation coincides with the development of the stem as the stem propagates forward towards the second island and begins to break. At this point, the developing stem runs up the island. As the run up recedes, (Fig. 4g) there is another interaction between the rundown, reflected wave and bifurcated wave crests. Video of the wave runup also shows areas of white water indicating breaking dissipation. From here, just as with the first island, (Fig. 4h–j) the bisected wave crests continue to propagate forward wrapping around the island and rejoin on the back side. The processes illustrated in panels (Fig. 4g–j) produce the radial estimate of maximum runup shown in Fig. 3.

Unlike with the first island however, the stem that develops on the onshore face of the second island propagates forward towards the beach without obstruction (Fig. 4k). Strong wave height gradients are present along the wave crest behind the island. Directly behind the island is a convergence of high wave energy density from the two crests rejoining, creating a stem and leading to a highly localized height maximum. Away from the island (y-DWB >> 0), the (far-field) wave is unaffected by transformation processes and remains a source of relatively high energy. A phase difference is observed between the developing stem and far-field wave crests, due to differences in celerity and propagation paths behind the island. The far-field segments of the wave run up the planar beach earlier than the stem wave behind the island. In some cases, the far-field segments have begun to recede as the wave stem initially propagates up the beach (Fig. 4l).

Profiles of maximum runup around the shoreward cone for Configuration A and Configuration B are shown in Fig. 5. The figure shows runup from the solitary wave (H = 0.14 m), error function wave and n_{max} wave, with all measurements taken at the 0.23 m water level. For all cases shown in Fig. 5, runup on the offshore face (θ = 0°) of the cone was greater than runup on the onshore face (θ = 180°). Runup results between 0° and 50° suggest imperfections in the cone construction lead to small perturbation in runup and a measurable variance in runup result. Runup on the onshore face was largest for the solitary wave. Runup produced by the error function and nmax wave are smaller and broader compared with the solitary wave. Video observations of the three waveforms suggest turbulent mixing produced by the error function wave and n_{max} wave results in a broadening of the onshore face runup.
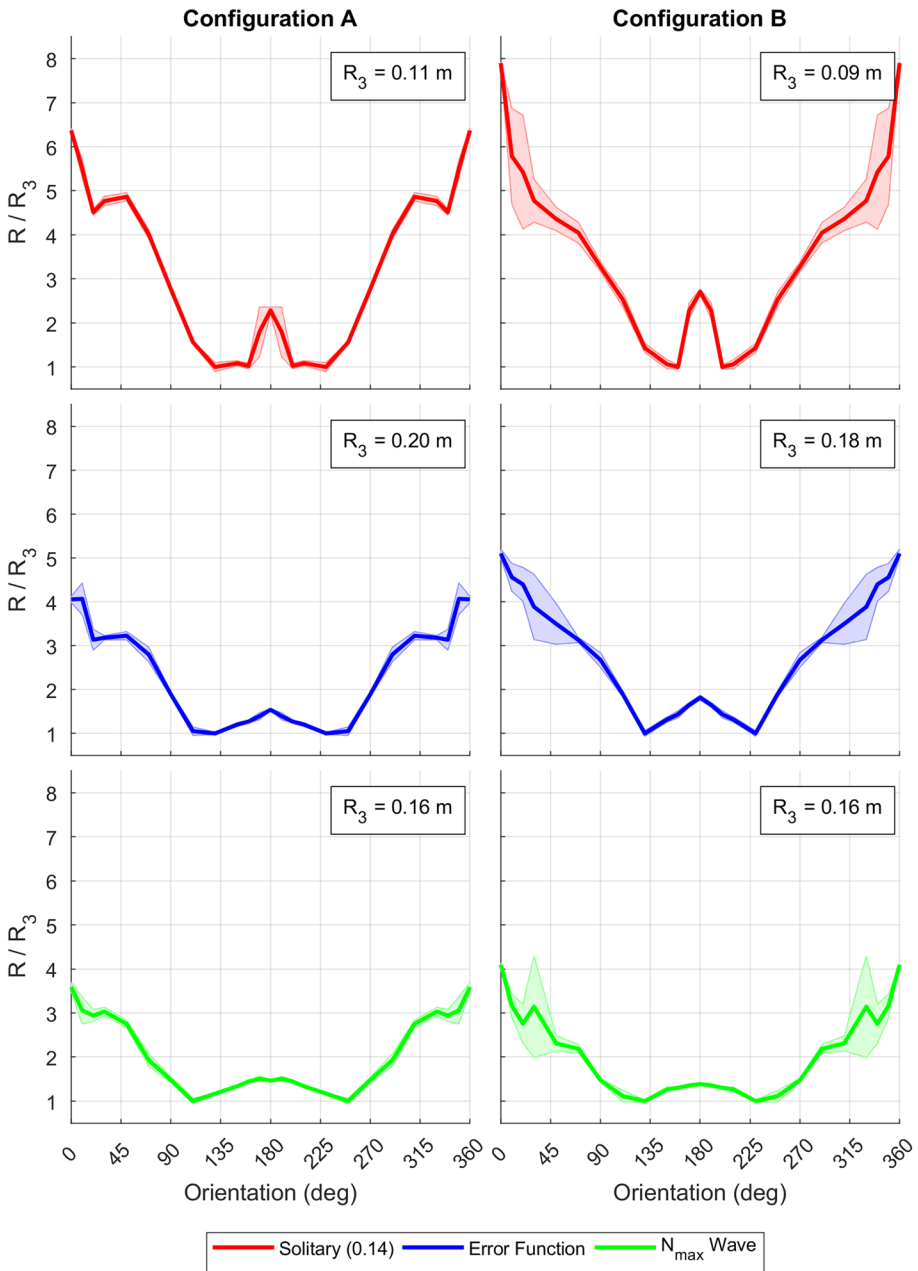
Fig. 5 Radial estimate of maximum runup (R) around shoreward cone for (left) Configuration A and (right) Configuration B at 0.23 m water level. The wave conditions include: (top) solitary wave (H = 0.14 m), (middle) error function wave and (bottom) n_max wave. The shaded regions show 90% confidence bounds
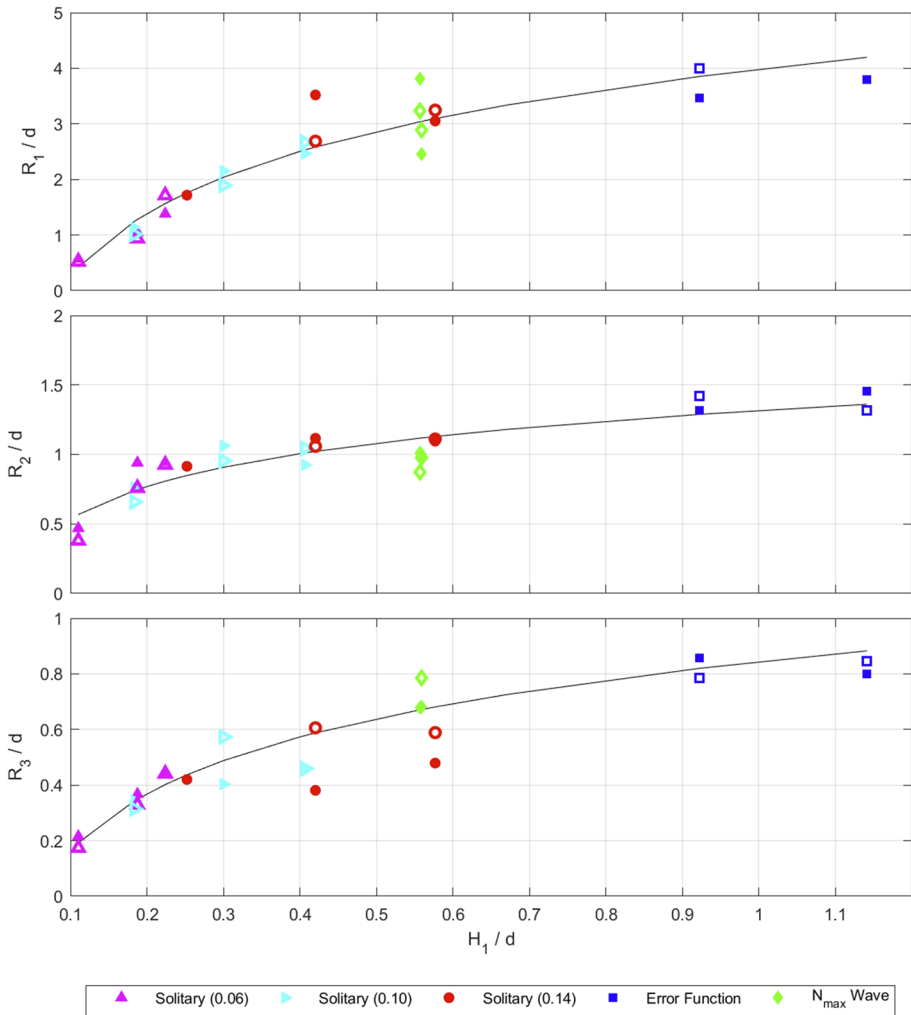
Fig. 6 The non-dimensional maximum wave runup versus the non-dimensional offshore wave height for Configuration A (full marker) and Configuration B (hollow marker). The maximum wave runup and offshore wave height were non-dimensional by water depth and include both breaking and non-breaking waves. The non-dimensional runup corresponds to (top) R_1, (middle) R_2 and (bottom) R_3. Wave height data was estimated at Resistance WG 01. Logarithmic data fit shown in each subplot

The non-dimensional maximum runup of waves versus the non-dimensional wave height for Configuration A and Configuration B is shown in Fig. 6. The top and middle panel represent non-dimensional runup maximums on the front and back side, respectively. The bottom panel represents the non-dimensional runup minimum. Ensemble and band averaged wave heights from the most offshore wave gauge (Resistance WG 01) were used to non-dimensional both the runup and water depth. The non-dimensional maximum wave runup (R_1/d) versus the non-dimensional offshore wave height is produced from phases in Fig. 4e–g.

The solitary wave data shown in Fig. 6 indicates a log-linear trend in solitary wave runup. The trend indicates that non-dimensional runup increases as the wave height over the water depth increase, a relationship related to the energy flux of the propagating wave. Observation from the video data indicates that the interplay between the developing stem and dissipation play an important role in defining the runup on the front side of the second island. Only a small amount of foamy, turbulent water was observed for the small solitary wave (H = 0.06 m) in 0.50 m water depth. A small amount of foamy, turbulent water should coincide with a small amount of dissipation. In contrast, a significant amount of dissipation was observed for the largest solitary wave (H = 0.14 m) in 0.23 m water depth. Video observations indicate that the solitary waves intermittently dissipate wave energy to equilibrate to the local bathymetry. The amount of dissipation largely dictates the runup on the front side of the second island.

The error function wave and n_{max} waveforms plotted in Fig. 6 indicate a log-linear trend in wave runup like the solitary wave. Note that data for these two waveforms are sparse since wave overtopping of the islands at intermediate (h = 0.30 m) and high (h = 0.50 m) water levels limited the recordable runup. The trend does indicate, even for the lowest water levels, that the n_{max} wave produces comparable runup to the largest solitary wave ($R_l/d \sim 3.3$). The error function wave produces the highest runup of the three waveforms, suggesting that runup is also related to wave period. Table 3 lists the wave time scales for each wave condition.
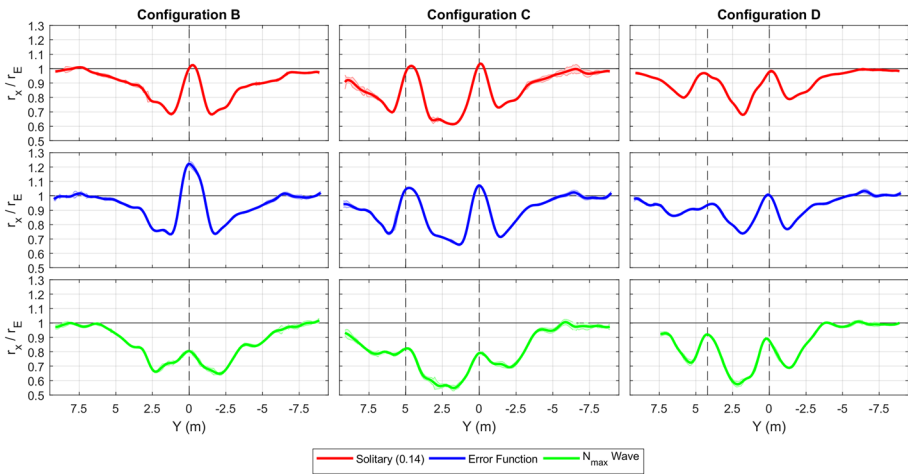
4 Planar beach runup

4.1 Data collection

Planar beach runup measurements were collected for Configurations B, Configuration C and Configuration D using two video cameras fixed atop the instrumentation carriage within the DWB. For more information on the data collection and post-processing, the reader is referred to Appendix 1. For each combination of waves and water levels, a total of eight estimates of maximum uprush were made. Since every camera view did not provide a complete estimate of the uprush limit, all the camera estimates were combined, band averaged and local outliers were removed. From this dataset a mean, standard deviation and number of degrees of freedom were estimated. These three metrics were used to establish the mean uprush limits as well as the 90% confidence bands which not only included variability in individual trials but also variability due to rectification error and local areas of low signal to noise ratio Fig. 7.

To summarize the 45 combinations of cone configuration, wave and water levels, a schematic representation of the planar beach runup was made. The schematic of runup is shown in Fig. 8. Only 5 points are needed to characterize the maximum runup for Configuration B. Points 1 and 5 represent how far the island's zone of influence reaches and are defined as points with runup equal to 95% of the no-offshore-island runup case (Configuration E). Points closest to 95% were used as the 95% value instead of interpolating. This resulted in a range of actual values between 90 and 100% for Points 1 and 5. In cases where the zone of influence extended beyond the field of view, the point was not included in the analysis. Points 2 thru 4 represent the local maximum and two minimum features characteristic to the runup. Also note that all runup lines have been nondimensionalized using the measured runup from the no-offshore-island case.
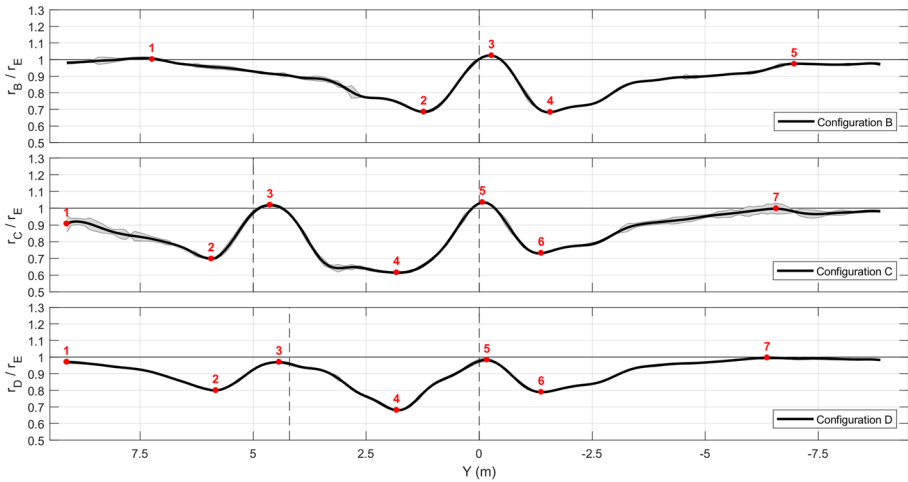
Fig. 7 Schematic of repetitive maximum and minimum points used to characterize the planar beach runup (r_X/r_E where X corresponds to the configuration) for (top) Configuration B, (middle) Configuration C and (bottom) Configuration D. These representative features can be identified across all solitary, error function and n_{max} wave waveforms. The shaded regions show representative 90% confidence bounds. Dashed lines indicate the approximate centerline of each island

Fig. 8 Estimate of nondimensional maximum runup (h = 0.30 m) on planar beach for (left) Configuration B, (middle) Configuration C and (right) Configuration D. The wave conditions include: (top) solitary wave (H = 0.14 m), (middle) error function wave and (bottom) n_{max} wave. The shaded regions show 90% confidence bounds. Dashed lines indicate the approximate centerline of each island

For Configuration C and D, 7 points are needed to characterize the maximum runup. Like Points 1 and 5 for Configuration B, Points 1 and 7 are the 95% limits which represent how far the island's zone of influence reaches. Points 2 thru 6 represent various local maximum and minimum features characteristic to the runup. Since there are two side by side island configurations, the added points are needed to characterize the two local maxima and various minima produced by each island.

4.2 Results and discussion

Profiles of maximum nondimensional runup on the planar beach for Configuration B, Configuration C and Configuration D are shown in Fig. 9. Average runup magnitudes from Configuration E are given in Table 3. In the figure r_X represents the runup which coincides with the configuration (e.g. r_B corresponds to the runup for Confirmation B). The plotted waves are the solitary wave (H = 0.14 m), error function wave and n_{max} wave, all shown at the 0.30 m water level. Figure 9 shows a clear difference in alongshore runup behavior between the solitary wave, error function wave and n_{max} wave. Of note, since the runup lines are non-dimensional, the local differences in wave dynamics are the focus of these plots. Comparisons between the runup magnitude can be dimensionalized using runup values for Configuration E from Table 3 but are not the focus here.

Wave propagation phases that produce the runup in Fig. 9 generally correspond to panels (i) through (k) in Fig. 4. While the general flow features show similarities across all waveforms, local flow features controlled by the wave characteristics result in local differences in nondimensional runup shown in Fig. 9. In Configuration B for example, solitary wave results indicate nominal wave runup ($r_B/r_E = 1.03$) whereas error function wave results exceeded unity ($r_B/r_E > 1.24$).

The continual presence of the breaking wave front indicates the error function wave is continually dissipating wave energy as it propagates. As the two wave fronts of the error function wave rejoin on the back side of the offshore island (Fig. 4e–f), the
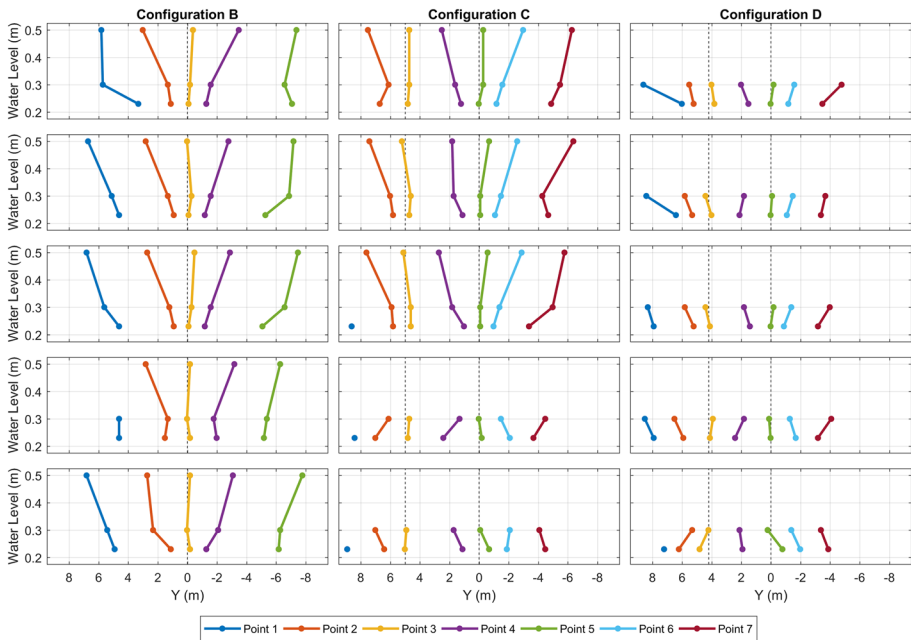
Fig. 9 Estimate of nondimensional alongshore maximum runup location (Y) on planar beach for (left) Configuration B, (middle) Configuration C and (right) Configuration D. The wave conditions include: (from top to bottom) a solitary wave (H = 0.06 m), a solitary wave (H = 0.10 m), a solitary wave (H = 0.14 m), an error function wave and a n_{max} wave. The shaded regions show 90% confidence bounds. Dashed lines indicate the approximate centerline of each island

nonlinear amplification of the developing wave stem locally increases the wave amplitude. This amplification appears to be greatest for the error function wave compared with the other modeled waveforms at this water depth, as indicated by the largest r_B/r_E among the examined wave types.

In contrast to the error function wave, results suggest the n_{max} wave produces a decrease of the wave runup ($r_B/r_E < 1$). Video data of the n_{max} wave once again reinforces the importance of the wave stem formation, shoaling, and dissipation. The n_{max} wave is the only waveform which propagates with an initial drawdown in water level. Locally behind the island, there is nonlinear amplification of the wave stem, like the solitary wave and error function wave. However, there are three main sources of dissipation in the n_{max} wave which appear to dominate over the nonlinear amplification. Firstly, the wave stem must propagate on top of an opposing current produced by the initial drawdown from the n_{max} wave. This draws energy out of the wave stem through dissipation. Secondly, the n_{max} wave stem also develops in shallower water depths compared with the solitary or error function waves because of the initial drawdown. This increases the relative importance of local depth dependent induced breaking. Video data also suggests that the stem breaks onto the shore as a collapsing breaker which locally and quickly draws energy out of the wave stem. Because of these three local dissipation mechanisms, the n_{max} wave runup is reduced just behind the island in contrast to both the solitary wave and error function.

Results from Fig. 9 also suggest the same processes occurring in Configuration B also appear to influence the results for Configuration C and Configuration D. The error function wave produces the highest runup peak magnitude, followed by the solitary wave and then the n_{max} wave. However, the emergence or submergence of the truncated cone appears to influence the second runup peak.

For the error function wave results for Configuration D, the second peak produced around y = 4 m is somewhat muted ($r_D/r_E = 0.95$) compared with the primary peak around y = 0 m ($r_D/r_E = 1.00$). At this water depth, the truncated cone is approximately equal to the water depth. Video footage of the run shows that the formation of the wave stem and dissipation on the backside of the truncated island is much smaller compared with the full island. Even though the truncated cone has some influence on the error function wave, as the truncated cone becomes more submerged with increasing water depths, the ability of the wave to wrap around the feature reduces and overtopping increases. Instead, the wave dissipates more energy and the stem that forms is small compared to the full cone, reducing the nondimensional runup magnitude compared with the full cone runup.

Estimates for non-dimensional maximum runup location on the planar beach for Configuration B, Configuration C and Configuration D are shown in Fig. 10. The figure provides data from: (from top to bottom) the solitary wave (H = 0.06 m), solitary wave (H = 0.10 m), solitary wave (H = 0.14 m), error function wave and n_{max} wave. Of note, some points are not present for the higher water levels for Configuration C and D. This is because at these water depths, the identifying maximal and minimal peak runup produced from the island configurations were small (< 5% variance from the mean nondimensional runup).

The runup trends are nearly the same for all wave conditions for Configuration B. As water level increases, the wave momentum flux increases which increases the lateral diffusion of energy along the beach. This causes the features to "spread" along the planar beach. The same trend can be observed for Configurations C and D for negative (y-DWB < 0) alongshore directions where no island is present. For positive alongshore directions (y-DWB > 0), the slope is less indicating that the trend is weaker. Most notably however are Points 3 and 5 which are the peaks of the two runup lines for each island. The data
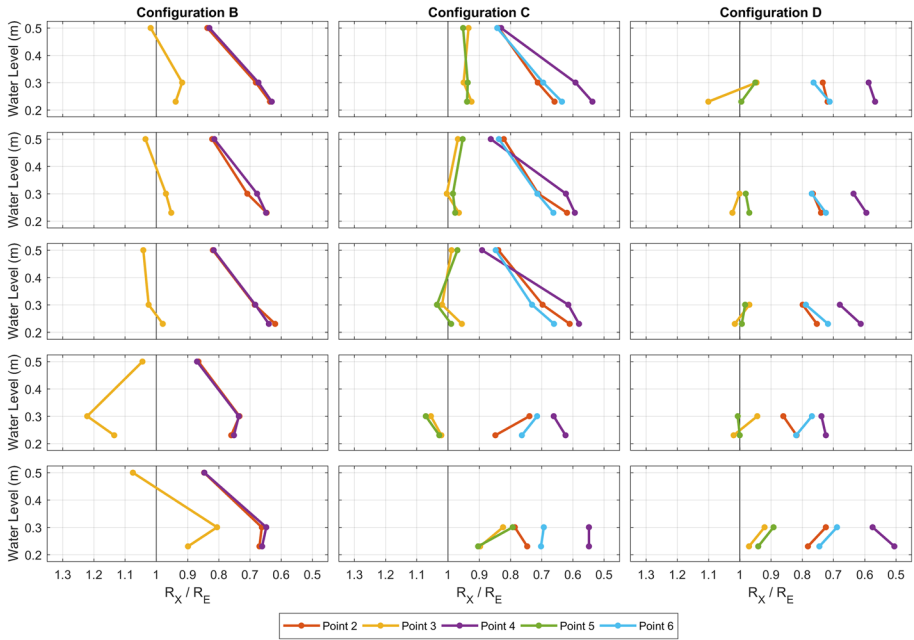
Fig. 10 Estimate of nondimensional cross-shore maximum runup height (R_X/R_E) on planar beach for (left) Configuration B, (middle) Configuration C and (right) Configuration D. The wave conditions include: (from top to bottom) a solitary wave (H=0.06 m), a solitary wave (H=0.10 m), a solitary wave (H=0.14 m), an error function wave and a n_{max} wave
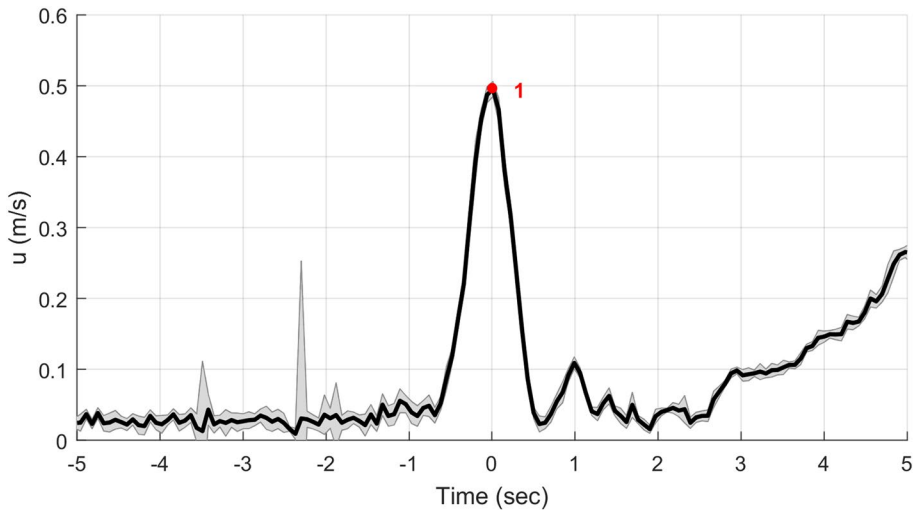
Fig. 11 Schematic of maximum velocity used to characterize the velocity (u) time series for all configurations. The shaded region shows representative 90% confidence bounds

indicates that the location of the peaks changes only slightly with water level relative to the minima and end points.

Estimates for non-dimensional cross-shore maximum runup location on the planar beach for Configuration B, Configuration C and Configuration D are shown in Fig. 11. Runup magnitudes from Configuration E are given in Table 3. The wave conditions include: (from top to bottom) a solitary wave (H = 0.06 m), a solitary wave (H = 0.10 m), a solitary wave (H = 0.14 m), an error function wave and a n_{max} wave. Points 1 and 5 for Configuration B and 1 and 7 for Configuration C and D are not included because their values are predefined.

The trends which were identified from Fig. 9 are nearly identical to those identified in Fig. 11 for other water levels. Conceptually, the error function and n_{max} wave can be thought of as producers of runup amplification ($R_x/R_E > 1$) and decrease in runup amplitude ($R_x/R_E < 1$), respectively due to their characteristic wave features. While the solitary wave is somewhere in between producing nearly normative ($R_x/R_E \sim 1$) runup. The one exception to this appears to be the higher water level for the n_{max} wave. A likely result of the higher water level decreasing the influence of the initial drawdown.

The symmetry of the configurations can also be identified in these results. For Configuration B, Points 2 and 4 represent the respective troughs. The two lines nearly overlapping each other indicates that the process to the positive and negative side of the DWB is symmetric. For Configuration C and D, Points 3 and 4 and Points 2 and 8 represent the peaks and troughs, respectively. The fact that they overlap indicates that the interference is nearly symmetric. For Configuration D where the lines don't overlap, would tend to indicate that the presence of the shorter truncated cone produces non-symmetrical wave dynamics and in turn interference patterns which are not symmetric between the two islands.

5 Planar beach current velocities

5.1 Data collection

Flow velocity measurements were collected for Configurations A–E using an ADV fixed to a metal frame just shoreward of the conical islands. The location of the ADV is shown in Fig. 1 and listed in Table 2. Every combination of island configuration, water level and waveform was repeated four times resulting in four realizations of the same velocity time series. Each realization required extensive cleaning to remove segments of data with a low signal to noise ratio. This process is discussed in detail in Appendix 1. Once the data was cleaned, dand and ensemble averaging resulted in a total of 40 data points from which a local mean, standard deviation and number of degrees of freedom were estimated. These three metrics were used to establish the 90% confidence bands. Once the mean and confidence limits were established, the peak velocity was estimated from each ensemble and band averaged velocity time series (see Fig. 12). A time offset was subtracted from the recorded time vector to align the maximum velocity with t = 0 s.

5.2 Results and discussion

Estimate of nondimensional flow velocity time series for Configuration A–E are shown in Fig. 13 for the 0.30 m water level. The wave conditions include a: solitary wave (H = 0.14 m), error function wave and n_{max} wave. The profiles have been non-dimensional against the maximum velocity magnitude from the no-island scenario (Configuration E)
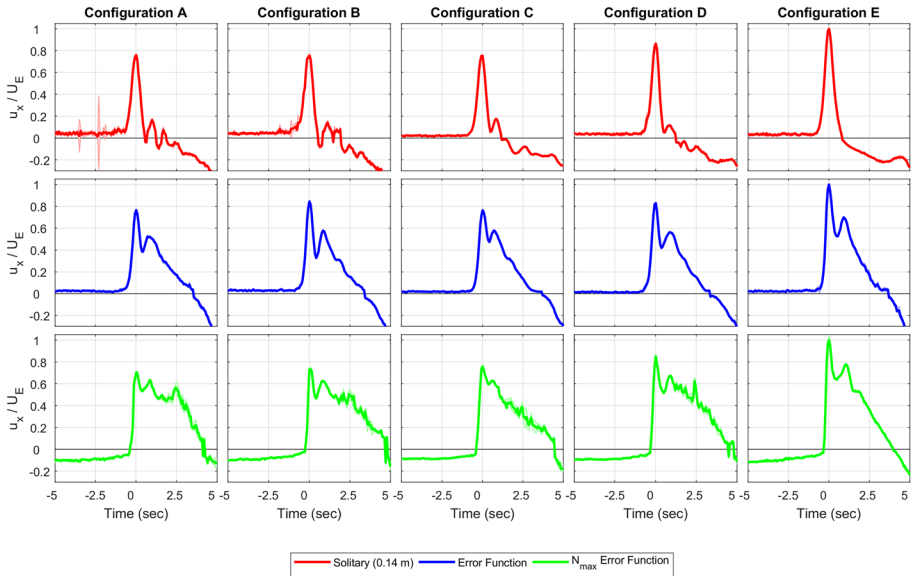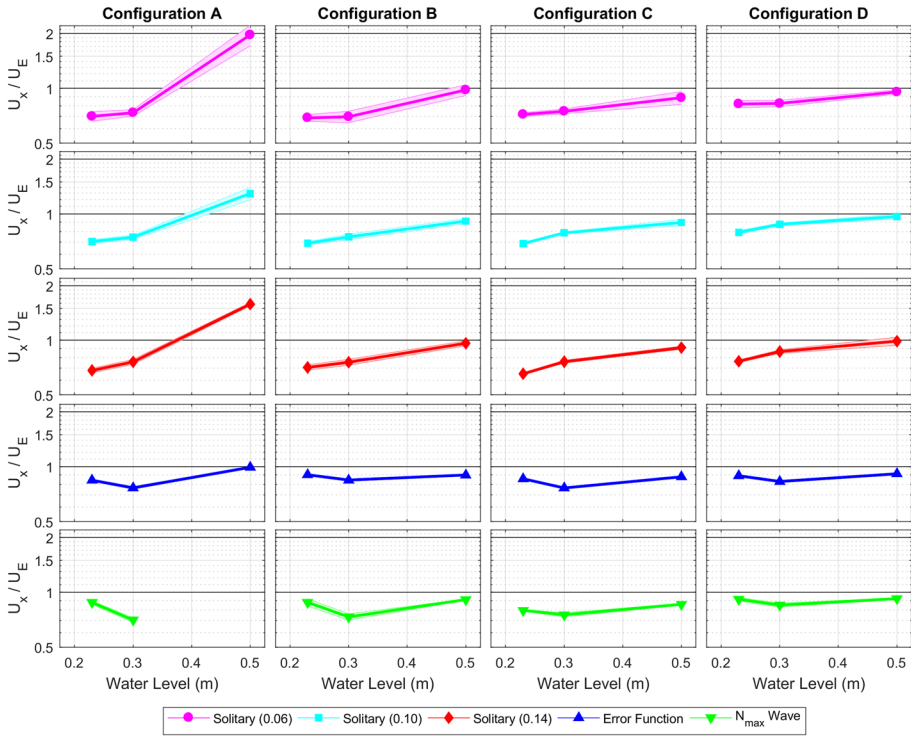
Fig. 12 Estimate of nondimensional flow velocity magnitude time series (h = 0.30 m) for (from left to right) Configuration A–E. The wave conditions include: (top) a solitary wave (H = 0.14 m), (middle) an error function wave ($T_1 = 5$) and (bottom) a n_{max} wave. Positive velocities are directed onshore, negative velocities are directed offshore. The shaded regions show 90% confidence bounds

and vary for each wave and water level condition. The velocity magnitudes for each wave and water level condition for the no-island scenario are listed in Table 3.

Figure 4 (panel i–k) correspond to the primary phases of wave propagation. Directly behind the island where the two crests rejoin, is an area of high wave energy which primarily controls the velocity time series at the ADV. Estimates of nondimensional flow velocity maximum magnitude for Configuration A–D are shown in Fig. 13. In the figure positive velocities are directed onshore while negative velocities are directed offshore. The median estimate of the ensemble and bin averaged directional data established the binary direction.

Results help illustrate the complex process which results from the joining wave fronts on the backside of the island and the nonlinear amplification of the developing stem. The solitary wave velocity trends in Fig. 14 for Configuration A and B show a clear increase in velocity magnitude with water depth even when nondimensionalized with the no-island case. The results suggest that as the celerity of the wave increases, the nonlinear amplification of the developing wave stem also increases with water depth. This amplification produces the locally higher celerity because of the amplification which is evident in the velocity data, indicated by the positive slope to the data.

The solitary wave trend in Fig. 14 between Configuration C and D show that current speeds for Configuration C were less than current speeds for Configuration D. Referring back to Fig. 1, the islands for Configuration D were smaller than the islands for Configuration C. The results demonstrate that island shielding is the predominant reason for the decrease in current magnitude (e.g. larger island block more wave energy). The larger offshore islands results in more refraction, diffraction and wave breaking which reduce the celerity of the incoming waves. This shielding effect is similarly observable in the error function and n_{max} wave results.

Fig. 13 Estimate of nondimensional flow velocity maximum magnitude for (from left to right) Configuration A–D
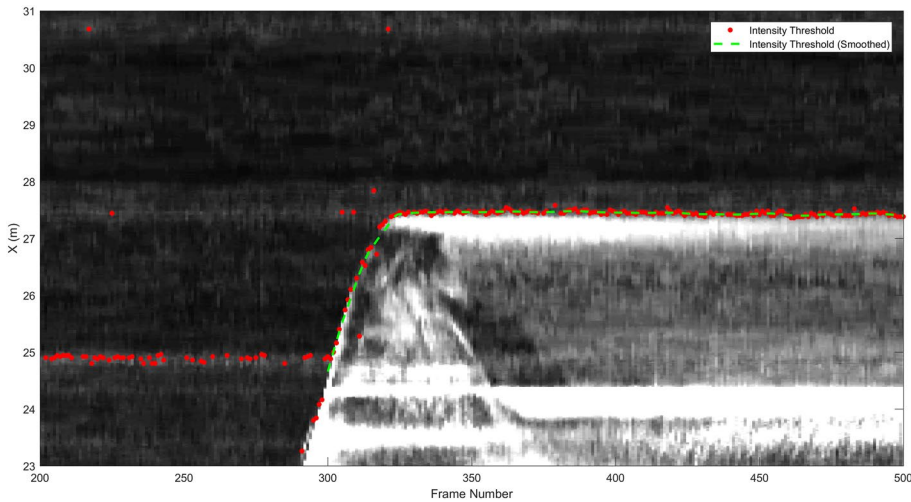
Fig. 14 Example variance transect of error function wave runup at the 0.23 m water level (Y = 0 m). Red dots indicate the shoreward limit of the variance threshold by frame number; the green line is the smoothed estimate of the variance threshold. The waveform enters the image at approximately frame 290 and reaches a maximum at approximately frame 325 before running down. Rundown is more difficult to detect then runup as the planar beach remains wet for a period after runup

6 Conclusions

The present study aimed to capture when and how island chains are amplifiers of wave energy in the coastal areas they shadow. Physical modeling was carried out in the DWB at the OSU O.H. Hinsdale Wave Research Laboratory. The experiment included four island configurations, three water depths and three waveforms. The modeled waveforms were comprised of a: solitary wave, error function wave and n_{max} wave.

The maximum runup around the shoreward cone for Configuration A and B was discussed in Sect. 3. The data, presented nondimensionally, indicated a log-linear trend in runup. The solitary wave trend showed that runup increases as the wave height and water depth increase; a relationship related to the energy flux of the propagating wave. The error function wave and n_{max} waveforms also plot along the log-linear runup trend but produce larger runup than the modeled solitary waves. The n_{max} wave produced the highest runup of the three waveforms, a consequence of the significantly larger wave time scale (i.e. longer waves producing higher runup values).

Section 4 discussed the runup profiles on the planar beach for Configuration B–D. Like the runup around the cone, all profiles were presented in a nondimensional manner, non-dimensionalized against the no-island scenario (Configuration E). While the general flow features show similarities across all profiles, local flow features controlled by the waveform characteristics resulted in local differences in nondimensional runup. The nondimensional runup amplification ($r_B/r_E > 1$) appeared to be greatest for the error function. Conversely, results suggest the n_{max} wave produces a decrease in the wave runup ($r_B/r_E < 1$). Video data indicate the reduction is mainly the result of the developing wave stem propagating over the opposing current produced from the n_{max} wave drawdown. This local intensification of the opposing current around the islands locally dissipates wave energy.

Estimates of nondimensional flow velocity maximum magnitude for Configuration A–D were summarized in Sect. 5. The solitary wave velocity trends for Configuration A and B show a clear increase in velocity magnitude with water depth. As the celerity of the wave increases, the nonlinear amplification of the developing wave stem also increases with water depth. The solitary wave trend between Configuration C and D show that current speeds for Configuration C were less than current speeds for Configuration D. Comparisons between these two configurations demonstrate that island shielding can play a role in decreasing the current magnitude.

These results and discussion show that island chains can act as wave amplifiers, indicating potential amplification in both shoreline runup and current velocity. The amplification is, however, not consistent with every waveform. Also, in some cases, the impact of the offshore islands led to a reduction in coastal impacts. This result suggests that the offshore waveform plays an important role in the wave dynamics between the islands and on the wave uprush directly behind the islands.

The data and discussion presented in this paper provides insight into long wave propagation and evolution around island chains. Additionally, the experiment could also be used as a dataset to calibrate and validate numerical models. While extrapolating to geophysical scale events should be done with caution, a few conclusions from the experimental results can be made. Firstly, while it is generally accepted that long wave runup is primarily driven by the upper beach slope (e.g. Synolakis [19]), results from this experiment indicate that shallow water offshore bathymetry also influences wave inundation. However, for this role to be significant (i.e. leading order) the island chains need to be strong and local, like the islands found in this experiment. Secondly, experimental results show that the waveform

can influence the wave inundation both in terms of the wave runup and current speed. Other factors that could influence wave inundation such as beach slope or distance of the island from the toe of the beach were not included as parameters in the experiment. These factors would fit nicely with future experiments (either physical or numerical) to further researchers understanding of long wave propagation and evolution around island chains.

Appendix 1: Data post-processing

Data was collected during the experiment to measure: conical island runup, planar beach runup and planar beach current velocities. Each data type required extensive post-processing. The post-processing procedure is discussed in this appendix.

Conical island runup

Conical island runup measurements were collected on Cone 1 (see Fig. 1) for Configurations A and Configuration B. To make this measurement, 24 vinyl measuring tapes were attached to the conical islands. Ten-degree spacing was used on the front and back ($330° \leq \theta \leq 30°$ and $150° \leq \theta \leq 210°$) while 20° spacing was used for the sides. The cones were orientated such that the 0° tape faced offshore while the 180° tape faced onshore. It is re-iterated that cone runup is only measured on the cone nearest to the shoreline; the runup on and wave evolution around the most-offshore cone should be similar to that investigated in Briggs et al. [13] and we see no reason to repeat that effort.

With each change in water level, a new zeroing of the measuring tapes was taken to establish a reference point for each runup measurement. Before each trial, the nearshore cone was wetted, and fine sand was dusted over the surface of the cone. The dried surface left an opaqueness to the cone which, once wetted again by the incipient wave, could be used to measure maximum runup around the circumference of the cone. After each run, a researcher would enter the water and visually estimate the wave runup at each tape. The cone was then wetted, and the process was repeated.

Planar beach runup

Planar beach runup measurements were collected for Configurations B, Configuration C and Configuration D using two video cameras fixed atop the instrumentation carriage within the DWB. The video cameras were not setup for Configuration A. Each camera recorded 1080p video at 30 Hz and was internally synced using a preprogramed LED light signal. The cameras were positioned to overlap the field of view of each camera. During the experiment, each camera was started by hand before the wavemaker motion and stopped at least 1 min after the maximum wave runup was reached.

To extract the maximum runup, the video frames needed to be rectified into basin coordinates. Forty-seven ground control points were selected in the basin within each camera field of view. The position of the ground control points within the basin were then extracted from lidar survey data taken during the experiment. The ground-control-point

locations were estimated by hand in each video frame and the pixel coordinates recorded. Each ground control point was averaged to estimate a mean position of the ground control point for each island configuration and field of view.

Using the MATLAB Image Processing Toolbox, a trivariate (rank of global mean, standard deviation and maximum error) minimization scheme was used to optimize each ground control point set by minimizing the rectification matrix error [20]. Once an estimate for the rectification matrix was made, each frame could then be rectified and interpolated into XY basin coordinates. The process is computationally intensive but somewhat more intuitive than attempting to estimate the wave runup in UV camera coordinates. In XY coordinates an independent estimate of wave runup can be made at each cross-shore transect. During this process, video frames were down sampled to 10 Hz and interpolated onto a grid of 0.01 m in the cross-shore direction and 0.05 m in the longshore direction.

A modified approach of Rueben et al. [21, 22] was used to estimate the line of maximum runup once the videos were rectified. First a basis frame was subtracted from the video frames. This basis frame was calculated as a mean of 50 frames at the start of each video, before the wave was generated. Once the basis frame was subtracted from a frame, what is left is known as a variance image [21]. The uprush of the wave's leading-edge can coincide with areas of strong variance intensity in the video time series (see Fig. 7). Unlike some techniques that depend upon a turbulent wave front to provide the strong contrast for feature tracking, this technique relies upon the contrast between the wet and dry surface. Since the overall waveform and inherent dynamics of a solitary wave, error function wave and n_{max} waves are different, this approach can accommodate the wide range of wave conditions.

Once a variance stack is estimated, a 2D median filter is passed through the data to remove local spikes in intensity that arise from non-flow features in the camera's field of view. Examples of local intensity spikes include light reflecting off the metal frame used to mount the ADV or a researcher walking on the beach and into the field of view during the run.

Edge tracking was done on a transect by transect basis. A threshold was selected which identifies the leading edge of the flow uprush. A locally weighted scatterplot (LOESS) filter was fit to the data to provide a continuous estimate of the leading runup edge in time. The point of maximum runup for each transect is estimated from the smoothed runup edge. An example transect from this process is shown in Fig. 7. Where this method deviates from Rueben et al. is in the iterative loop included in the transect front tracking [20]. Using a 3-sigma approach (described in more detail in Sect. 5), a maximum uprush limiter was included which minimized the variance of the uprush limit. Since maximum uprush is an inherently unstable statistic vulnerable to outliers, this added iterative loop helps to remove outliers from the maximum runup.

Planar beach current velocities

Flow velocity measurements were collected for Configurations A–E using an ADV fixed to a metal frame just shoreward of the conical islands. Prior to each run, a researcher added a slurry of seed material to the water around the instrument and mixed the water by hand to incorporate the material thought the water column. In natural water bodies, the natural occurrence of particles is sufficient for proper ADV operation. However, in clean, quiescent water like the DWB, seeding materials must be added to the water for proper ADV

operation. Even with the addition of seed material, however, ADV data must be extensively cleaned to provide reliable data.

Each individual velocity time series was initially cleaned using the beam correlation and signal-to-noise ratio provided by the ADV manufacturer. Once the initial pass was done, a 3-sigma filter was used to remove outliers not identified by the beam strength and signal-to-noise ratio. A 3-sigma filter uses a low-pass filter to establish a long period wave shape. The long period trend is then subtracted from the velocity time series resulting in two data sets: a low frequency (long period wave shape) and high frequency time series. The high frequency time series was used to estimate a mean and standard deviation. From the statistical estimate, thresholds of three standard deviations above or below the long period trend removed outliers from the velocity time series.

Every combination of island configuration, water level and waveform was repeated four times resulting in four realizations of the same velocity time series. Once outliers were removed from each individual velocity time series, the time series from each run were collected into common data sets. Each time series within the set, however, did not start at the same time. The velocity time series start only roughly corresponded with the start of the wavemaker. An approach needed to be developed to correlate the individual time series within each set. In other words, time shifts needed to be estimated to align each individual time series within the set with a common time datum.

A template matching approach correlated velocities between individual velocity time series within a single data set. Initially, a visual inspection of each velocity time series identified the time series with the lowest variance and least number of data gaps. This time series was used as the "template" for the data set. The second time-series from the dataset was added to the analysis and positive and negative phase lags were introduced between the template time series and second velocity time series. The result of this analysis is a time series of phase lag versus correlation. As the phase lags increase/decrease from zero, the correlation fluctuates between zero and one eventually reaching a maximum somewhere between ± 30 s lag. The highest correlation from the phase lag versus correlation time series was used as the best estimate of phase lag between the template velocity time series and individual time series. The template matching processes was repeated for the third and fourth time series. Researchers visually inspected the phase shifted velocity time series data set to ensure reasonable agreement between runs. A template matching approach is advantageous as it allows for each data set to be both band and ensemble averaged to increase the confidence in each individual estimate. While the data was cleaned, some local outliers and data gaps did still exist and were incorporated into the final velocity estimate via band and ensemble averaging.

Appendix 2: Wavemaker trajectories

The wavemaker trajectories are described in this appendix. The trajectories for the solitary wave (H$=0.14$ m), error function wave and n_{max} wave shown in Fig. 15 (for the 0.30 m water level). For the solitary wave, the wavemaker trajectory is described as positive forward stroke of the wavemaker with approximately 20 s of no wavemaker movement before and after the forward stroke. The wavemaker trajectory for the solitary wave changes based upon the desired wave height and water level condition. As the water level increases, the wavemaker stroke magnitude must also increase to achieve the same wave height for all
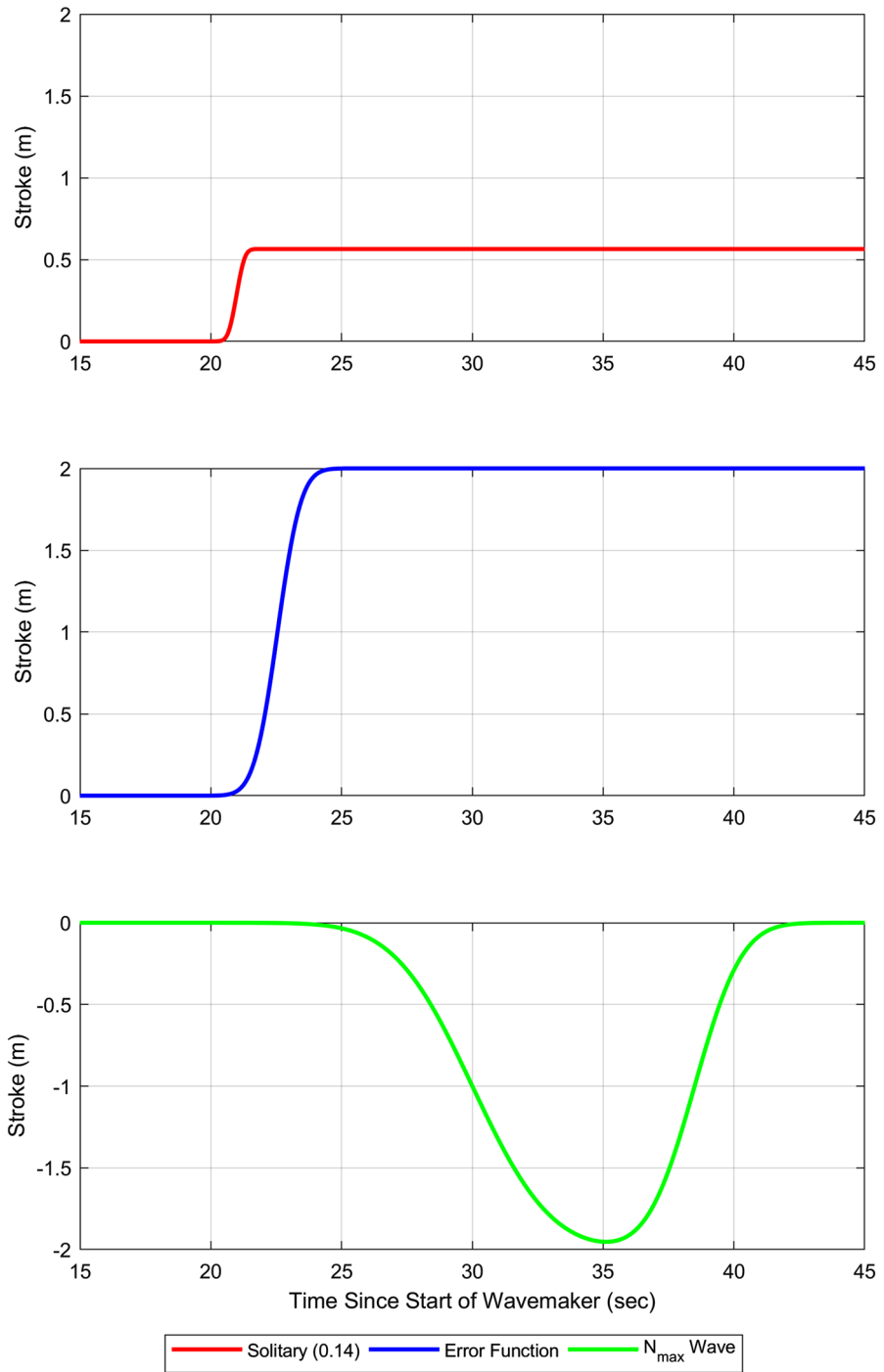
Fig. 15 Wavemaker trajectories used for the physical modeling: (top) solitary wave (H=0.13 m), (middle) error function wave and (bottom) n_{max} wave. Trajectories are for the 0.30 m water level

three water depths. Figure 15 only shows the wavemaker trajectory for one wave height and water level conditions (H = 0.20 m and h = 0.23 m).

Unlike the solitary wave trajectory, the wavemaker trajectory for the error function and n_{max} waves are identical for all water levels. The wavemaker trajectory for the error function wave is described as a positive forward stroke of the wavemaker with approximately 20 s of no wavemaker movement before and after the forward stroke (like the solitary wave). The wavemaker trajectory for the n_{max} wave is characterized by an initial drawback of the wave paddle followed by a positive forward stroke with no wavemaker movement before and after the paddle movement. The initial position of the n_{max} wave paddle is fully extended to accommodate the initial drawback of the wave paddle. Note that the initial position for the n_{max} wave differs from the initial position of the paddle for the solitary and error function waves. For these two waveforms. the paddle position is initially fully retracted.

References

1. Hill EM, Borrero JC, Huang Z et al (2012) The 2010 Mw 7.8 Mentawai earthquake: very shallow source of a rare tsunami earthquake determined from tsunami field survey and near-field GPS data. J Geophys Res Solid Earth. https://doi.org/10.1029/2012JB009159
2. Liu PL-F, Lynett P, Fernando H et al (2005) Observations by the international tsunami survey team in Sri Lanka. Science 308:1595. https://doi.org/10.1126/science.1110730
3. Titov V, Rabinovich AB, Mofjeld HO et al (2005) The global reach of the 26 December 2004 Sumatra tsunami. Science 309:2045. https://doi.org/10.1126/science.1114576
4. González FI, Milburn HB, Bernard EN, Newman J (1998) Deep-ocean assessment and reporting of tsunamis (DART): brief overview and status report. In: Proceedings of the international workshop on tsunami disaster mitigation, pp 118–129
5. Green DS (2006) Transitioning NOAA moored buoy systems from research to operations. In: Proceedings of MTS/IEEE OCEANS, Boston, MA, USA, pp 1–3
6. Meinig C, Stalin SE, Nakamura AI, Milburn HB (2005) Real-time deep-ocean tsunami measuring, monitoring, and reporting system: the NOAA DART II description and disclosure. Pacific Marine Environmental Laboratory, pp 1–15
7. Milburn HB, Nakamura AI, Gonzalez FI (1996) Real-time tsunami reporting from the deep ocean. In: Proceedings of MTS/IEEE OCEANS, pp 390–394
8. Mofjeld H (2008) Deep-ocean assessment and reporting of tsunamis (DART): tsunami detection algorithm. https://www.ndbc.noaa.gov/dart/algorithm.shtml. Accessed 28 Aug 2018
9. National Ocean and Atmospheric Administration (2017) Deep-ocean assessment and reporting of tsunamis (DART®) description. https://www.ndbc.noaa.gov/dart/dart.shtml. Accessed 28 August 2018
10. Stefanakis TS, Contal E, Vayatis N et al (2014) Can small islands protect nearby coasts from tsunamis? An active experimental design approach. Proc R Soc Math Phys Eng Sci. https://doi.org/10.1098/rspa.2014.0575
11. Yeh H, Imamura F, Synolakis C et al (1993) The Flores Island tsunamis. EOS Trans Am Geophys Union 74:369–373. https://doi.org/10.1029/93EO00381
12. Yeh H, Liu P, Briggs M, Synolakis C (1994) Propagation and amplification of tsunamis at coastal boundaries. Nature 372:353. https://doi.org/10.1038/372353a0
13. Briggs M, Synolakis C, Harkins G, Green D (1995) Laboratory experiments of tsunami runup on a circular island. Pure Appl Geophys 144:569–593. https://doi.org/10.1007/BF00874384
14. Liu PL-F, Cho Y-S, Briggs MJ et al (1995) Runup of solitary waves on a circular island. J Fluid Mech 302:259–285. https://doi.org/10.1017/S0022112095004095
15. Satake K, Nishimura Y, Putra PS et al (2013) Tsunami source of the 2010 Mentawai, Indonesia earthquake inferred from tsunami field survey and waveform modeling. Pure Appl Geophys 170:1567–1582. https://doi.org/10.1007/s00024-012-0536-y
16. Madsen PA, Fuhrman DR, Schäffer HA (2008) On the solitary wave paradigm for tsunamis. J Geophys Res Oceans. https://doi.org/10.1029/2008JC004932
17. Tadepalli S, Synolakis CE (1994) The run-up of N-waves on sloping beaches. Proc R Soc Lond Ser Math Phys Sci 445:99. https://doi.org/10.1098/rspa.1994.0050

18. Tadepalli S, Synolakis CE (1996) Model for the leading waves of tsunamis. Phys Rev Lett 77:2141–2144. https://doi.org/10.1103/PhysRevLett.77.2141

19. Synolakis CE (1987) The runup of solitary waves. J Fluid Mech 185:523–544. https://doi.org/10.1017/S002211208700329X

20. The MathWorks Inc (2018) Image processing toolbox. The MathWorks Inc. https://www.mathworks.com/products/image.html. Accessed 29 Aug 2018

21. Rueben M, Holman R, Cox D et al (2011) Optical measurements of tsunami inundation through an urban waterfront modeled in a large-scale laboratory basin. Coast Eng 58:229–238. https://doi.org/10.1016/j.coastaleng.2010.10.005

22. Rueben M, Cox D, Holman R et al (2015) Optical measurements of tsunami inundation and debris movement in a large-scale wave basin. J Waterw Port Coast Ocean Eng 141:04014029. https://doi.org/10.1061/(ASCE)WW.1943-5460.0000267